Editors' Suggestion

Symmetry Breaking in the Superionic Phase of Silver Iodide

Amir Hajibabaei,[1,*] William J. Baldwin,[2] Gábor Csányi,[2] and Stephen J. Cox[1,3,†]
[1]Yusuf Hamied Department of Chemistry, University of Cambridge, Cambridge CB2 1EW, United Kingdom
[2]Engineering Laboratory, University of Cambridge, Cambridge CB2 1PZ, United Kingdom
[3]Department of Chemistry, Durham University, South Road, Durham DH1 3LE, United Kingdom

(Received 18 June 2024; accepted 19 November 2024; published 17 January 2025)

In the superionic phase of silver iodide, we observe a distorted tetragonal structure characterized by symmetry breaking in the cation distribution. This phase competes with the well known bcc phase with a symmetric cation distribution, at an energetic cost of only a few meV/atom. The small energy difference suggests that these competing structures may both be thermally accessible near the superionic transition temperature. We also find that the distribution of silver ions depends on the low-temperature parent polymorph, with memory persisting in the superionic phase on the nanosecond timescales accessible in our simulations. Furthermore, simulations on the order of 100 ns reveal that even at temperatures where the bcc phase is stable, significant fluctuations toward the tetragonal lattice structure remain. Our results are consistent with many "anomalous" experimental observations and offer a molecular mechanism for the "memory effect" in silver iodide.

DOI: 10.1103/PhysRevLett.134.026306

Solid electrolytes offer great promise as materials for energy storage owing to their excellent ionic conductivity, with relatively high energy densities while remaining safe to use. But the atomic mechanisms that govern their behavior are far from simple [1]. For example, nanoscale diffusion in superionic conductors can substantially differ from the typical Brownian motion [2–8]. The archetypal type I solid electrolyte used as a model to understand these systems is silver iodide [9], yet many of its properties remain poorly understood [10].

At ambient conditions, AgI assumes hexagonal/cubic close-packed structures with many possible polymorphs resulting from variations in the stacking sequence. The main polymorphs with ordered stacking sequences are wurtzite (β) and zincblende (γ) [11–13]. Heated above 147 °C, a β/γ mixture transitions into the superionic α phase with a bcc I^- framework. It is known, from nearly a century ago [14], that the α phase can retain a memory of its parent structure evident from the β/γ composition obtained upon cooling. This "memory effect" was systematically investigated more recently [15] by heating and cooling samples with well-controlled degrees of stacking disorder, which showed that the degree of persisting memory also depends on kinetic factors such as the cooling rate. As the $\beta/\gamma \rightarrow \alpha$ transition occurs rapidly and with no remaining traces of the low-temperature phases, mechanisms such as nucleation and crystallization are generally ruled out.

Although a clear explanation for this memory effect has remained elusive, there is ample evidence to suggest that the picture painted by the notion of a straightforward $\beta/\gamma \rightarrow \alpha$ phase transition is too simplistic [14–16]. For example, it has been proposed that Ag^+ ions preferentially occupy certain sites within the I^- bcc framework, and that the degree of preference for certain sites depends upon the β/γ stacking composition of the low-temperature parent phase [16]. In this seminal study of the memory effect, Burley proposed that such preferential site occupation was responsible for sample-dependent variations in integrated intensities of the diffraction pattern in the α phase. Moreover, he also noted that any memory is irreversibly lost when temperatures exceed 170–175 °C.

Experiments at higher temperatures further demonstrate AgI's complex phase behavior. For example, at approximately 427 °C, AgI undergoes a further order-disorder transition, which, in purely stoichiometric samples, exhibits an anomalous heat capacity [17,18]. In a subsequent theoretical analysis, Perrott and Fletcher attribute this observation to entropic changes, of which the configurational entropy of Ag^+ plays a major role [19]. Early Raman spectroscopy experiments generally support this scenario [20–23]. More recent Raman polarization-orientation measurements [24] on single crystals of the α phase found crystal-like features that could not be accounted for solely by the bcc I^- host lattice, nor by assuming a crystal-like average distribution of the mobile Ag^+. Instead, this

*Contact author: ah2281@cam.ac.uk
†Contact author: stephen.j.cox@durham.ac.uk

observation was attributed to strongly anharmonic I^- lattice vibrations that are coupled to Ag^+ diffusion.

Molecular simulations are in principle well placed to provide insight at the microscopic level to help understand such experimental observations. Indeed, classical molecular dynamics (MD) simulations employing the empirical Parrinello-Rahman-Vashista force field [25,26] support the notion of Ag^+ preferentially occupying sites in the α phase [27–31]. Despite considerable constraints on the time and length scales that can be probed, insights from *ab initio* MD (AIMD) simulations [32] elucidate a dynamic bonding behavior that is challenging to capture with conventional empirical force fields. In particular, recent work has shown that iodide's lone pair of electrons, represented by maximally localized Wannier centers, have a rotational motion that couples to diffusion of Ag^+ [33], in an analogous manner to the "paddle-wheel" mechanism associated with molecular superionic solids.

To overcome the limits on accessible timescales and length scales imposed by AIMD approaches, here we exploit recent advances in developing machine learning interatomic potentials (MLIPs) to train a surrogate model that represents the underlying potential energy surface (PES) [34,35], as determined by the Perdew-Burke-Ernzerhof (PBE) functional [36], with dispersion interactions included using Grimme's D3 correction [37] with Becke-Johnson damping [38]. QUANTUM ESPRESSO [39–41], along with the pseudopotentials Ag/I. pbe-n-kjpaw-psl.1.0.0.UPF taken from PSLibrary v1.0.0 [42], was used for all DFT calculations. The density functional theory (DFT) settings are discussed further in the Supplemental Material [43].

For the MLIP, we employ the MACE architecture [49,50] to represent the PES. For training, we employed an active learning procedure with a committee of five MACE models. The majority of the training data comprises configurations derived from the wurtzite/zincblende and rocksalt crystal structures by active learning, though in addition we also included structures derived from other crystal structures found in the *Materials Project* online database [51]. In the temperature range of interest for this Letter, $270 \leq T/\mathrm{K} \leq 450$, the model demonstrated an accuracy with a root mean squared error of less than (1 meV/atom, 13 meV/Å) for (energy, force) predictions. Further information on training and testing is discussed in the Supplemental Material [43].

With the trained MLIP, we perform simulations that probe the memory effect. Specifically, we use isothermal-isobaric (NPT) MD simulations at a pressure $P = 0$ GPa, and at a variety of temperatures (T), starting from either the wurtzite or zincblende crystal structures, and analyze how the resulting structures depend upon the initial configuration. The simulation cell comprised twelve 8×8 Ag-I double layers with hcp/fcc stacking sequences to construct wurtzite/zincblende structures with 1536 atoms. Temperature and pressure were maintained with a Nosé-Hoover thermostat and Parrinello-Rahman barostat, respectively, as implemented in the ATOMIC SIMULATION ENVIRONMENT Python package [52,53].

Results for the computed self diffusion coefficients D for Ag^+ are presented in Fig. 1(a). For both the wurtzite- and zincblende-derived trajectories, we observe a jump in D at $T \approx 340$ K, and a second increase at $T \approx 370$ K. We also observe that our computed values for D are broadly in line with experiment [54], albeit offset by approximately 70 K [55]. Shifting the experimentally observed transition temperature (i.e., $420\ \mathrm{K} - 70\ \mathrm{K} = 350\ \mathrm{K}$) by the same amount agrees well with the observed initial jump in D.

Representative snapshots of structures at different temperatures are shown in Fig. 1(b). For $T \gtrsim 370$ K, space group analysis of the average iodide positions confirms the expected bcc framework of the α phase [56], with lattice constant $a = 5.06$ Å. For $340 \lesssim T/\mathrm{K} \lesssim 370$, however, we instead observe distorted lattice structures. The distortions are such that the repeat unit can be described as a $2 \times 2 \times 2$ superstructure of a body-centered tetragonal lattice with space group I4/mmm (see Fig. S3 [43]). Although their distortions differ, the underlying tetragonal lattices of the iodide framework in this temperature range are largely similar whether derived from wurtzite or zincblende, with lattice constants $a \approx 4.79$ Å and $c \approx 5.58$ Å. (Across this temperature range, a and c vary by approx. 0.002 Å.) We refer to such distorted tetragonal structures hereafter as tet′, with subscripts to indicate the parent phase when needed (i.e., $\mathrm{tet}'_{\mathrm{wz}}$ from wurtzite, and $\mathrm{tet}'_{\mathrm{zb}}$ from zincblende). At temperatures slightly below, but close to the superionic transition, we observe structures in which the iodide framework is slightly distorted from the underlying parent phase, but with significant rearrangement of the Ag^+ ions. For wurtzite, these structures are observed for temperatures $320 \lesssim T/\mathrm{K} \lesssim 330$, while for zincblende they occur across a wider range, $300 \lesssim T/\mathrm{K} \lesssim 330$. Ag^+ diffusivity below 340 K is further discussed in the Supplemental Material [43].

While the distortions of the iodide frameworks in the tet′ structures show relatively minor dependence on the parent phase, differences in the distribution of the Ag^+ ions are clear from a visual inspection of the trajectories. To further analyze this observation, we performed MD simulations of $\mathrm{tet}'_{\mathrm{wz}}$ and $\mathrm{tet}'_{\mathrm{zb}}$ at $T = 350$ K, with the volume fixed at the average from the NPT simulations. We also performed a similar simulation for the bcc structure at $T = 390$ K. The length of these simulations was 4–6 ns. The calculated histograms of Ag^+ positions are shown in Fig. 1(c) for various slices in the ab plane at different values along the c axis.

Consistent with the experimental consensus [56–59], we observe peaks in the Ag^+ density at the tetrahedral sites [$(0, 1/2, 1/4)$ etc.] in the bcc phase, with a slight spreading toward the octahedral sites [$(0, 1/2, 0)$ etc.]. On the other hand, translational symmetry is broken in the tet′ phases, as

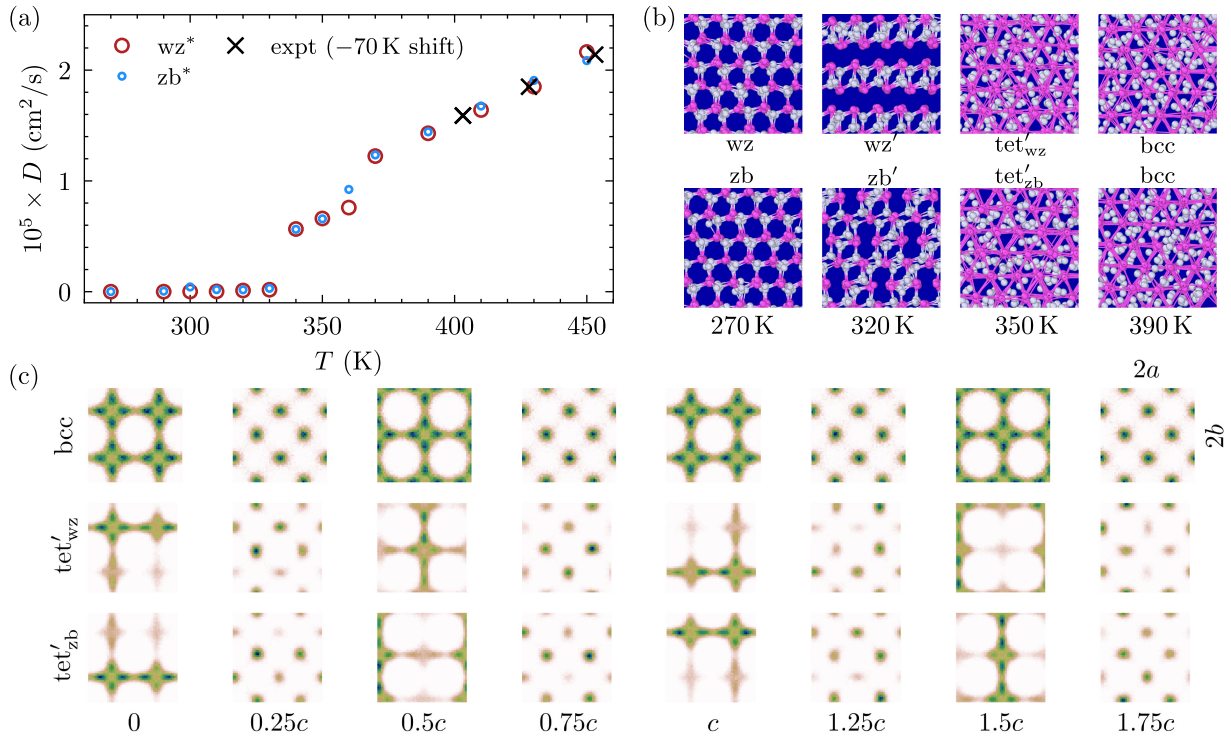

FIG. 1. The phase changes of AgI at $P = 0$ GPa derived from wurtzite (wz*) and zincblende (zb*) configurations. (a) Self diffusion constants of Ag^+ indicate a superionic transition at $T \approx 340$ K in the simulations. The diffusion constants from simulation are in good agreement with experimental data [54], once a 70 K shift is accounted for. (b) Snapshots at different temperatures (as indicated) show intermediate structures between wz*/zb* and the expected bcc lattice for the superionic phase. Note that only part of the simulation cell is shown for clarity. (c) The Ag^+ distributions are shown by cross sections along the c axis. For the distorted tetragonal lattices tet'_{wz} and tet'_{zb} at 350 K, the Ag^+ distribution has a broken symmetry which depends on the low-temperature parent phase. The site occupation symmetry is recovered in the bcc phase at 390 K.

reflected in the asymmetric occupation of the tetrahedral sites. Significant differences between the two become further apparent upon investigation of the connectivity of maxima in the Ag^+ distributions, as seen in Fig. S4 in the Supplemental Material [43].

Based on an analysis of x-ray diffraction data, Burley proposed that differences in the Ag^+ distributions in the high temperature phase play a determining role in the memory effect [16]. Our simulation results potentially lend support to such a hypothesis. To probe this notion further, for both wurtzite and zincblende as initial structures, we generated an ensemble of eight independent trajectories of 1 ns at $T = 350$ K and $P = 0$ GPa, and a further eight each at $T = 390$ K. Following this initial NPT trajectory, NVT simulations of 1 ns were performed using the average cell parameters, from which the structure factors, $S(|\vec{k}|)$, were calculated. These are presented in Fig. 2.

At 350 K the peaks in $S(\vec{k})$ deviate from the ideal tetragonal lattice owing to the persistent distortions in the I^- framework. Of particular note is a "superstructuring" peak at $|\vec{k}| \approx 0.87$ Å^{-1}, which is indicative of long-range ordering of the Ag^+ (see partial structure factors in Fig. S6 [43]). A trace of this superstructuring peak persists in the bcc phase at 390 K, at least on the nanosecond timescales accessible in our simulations. Importantly, similar to Burley's observations, the intensities of the peaks consistent with the bcc framework are different for the wurtzite- and zincblende-derived structures. In addition, at $|\vec{k}| \approx 3.93$ Å^{-1}, corresponding to Miller indices [3, 1, 0], there is a minor peak present for the wurtzite-derived structure that is absent in that derived from zincblende. Thus, on the timescales and length scales accessible in our simulations, the bcc structures we observe retain memory of their low-temperature parent phase.

While Burley mentions a splitting of the diffraction pattern near the transition temperature consistent with a tetragonal cell, we are not aware of clear experimental evidence of this structure. Therefore, to better understand the tet′ structures and their relationship to the bcc phase, we performed a set of simulations with a smaller system size at $P = 0$ GPa and $T/\mathrm{K} = 350, 365, 390$. Specifically, we initialize the system with a $4 \times 4 \times 4$ bcc iodide framework, and randomly distribute the Ag^+, while avoiding unphysical overlap. Using this smaller system size allows us to sample over timescales exceeding 100 ns. In Fig. 3, we show histograms of $\ell_\nu = L_\nu/4$, where L_ν is the simulation

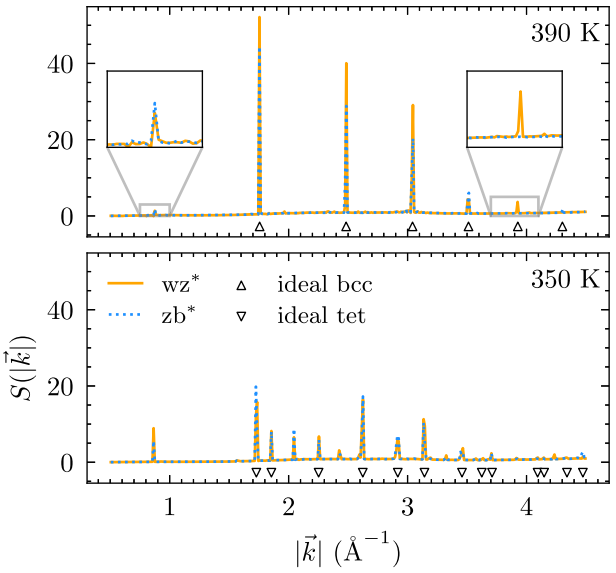

FIG. 2. Memory persists in the superionic phase, as indicated by the structure factors obtained from an average of eight simulations. A "superstructuring" peak at $\vec{k} \approx 0.87$ Å^{-1} is observed in the distorted tetragonal lattices at 350 K (lower panel) which is also observed in the predominantly bcc lattice at 390 K (upper panel). A peak at $\vec{k} \approx 3.93$ Å^{-1} is also observed at 390 K for structures derived from wurtzite (wz*), which is absent for structures derived from zincblende (zb*). In addition, the peak intensities at 390 K differ between the wurtzite and zincblende derived structures. The expected patterns from ideal bcc and tetragonal (with space group I4/mmm) lattices are shown as a guide, as indicated by the legend.

cell length along $\nu \in (x, y, z)$, along with their respective time series shown in the insets.

At 350 K, we immediately see that the system transforms into a tetragonal lattice, with lattice parameters consistent with our earlier space group analysis. However, we also see that the direction of the c axis flips between x, y, and z, which corresponds to switching the mode of symmetry breaking in the Ag^+ distribution (see Fig. S7 [43]). Given this observed flipping of the c axis, we might expect the averaged structure to resemble, over sufficiently long times, the bcc lattice with $\ell_x = \ell_y = \ell_z$. However, the histograms presented in Fig. 3 indicate that the c axis preferentially aligns along the x axis. Despite the computational efficiency of the MLIP compared to AIMD, probing longer timescales and length scales remains too computationally demanding, and we therefore cannot conclude definitively whether these observations correspond to (i) a genuine breaking of ergodicity or (ii) a relevant timescale that exceeds the length of our simulations. While either could provide a mechanism for the memory effect, scenario (ii) seems in line with experimental diffraction patterns that show bcc symmetry, and the observation that the memory effect depends on kinetic factors such as the cooling rate [15,16].

For a closer analysis of these lattice structures, we assign (a, b, c) to sorted $\{\ell_\nu\}$ such that $a \leq b \leq c$ at every instance. We can then quantify the degree of spontaneous tetragonal distortion by $2c/(a+b)$. The joint probability density of $2c/(a+b)$ with the potential energy per atom u is presented in Fig. 3 which confirms that tetragonal lattices dominate at 350 K and bcc lattices at 390 K. At both temperatures, however, the probability densities indicate significant populations of the competing lattice structure. For the intermediate temperature of 365 K, both bcc and tetragonal lattices are observed with significant probabilities, with the tetragonal lattice lower in potential energy by approximately 5 meV/atom. This suggests that the bcc lattice is stabilized by entropic effects. While confirming with appropriate finite size scaling remains too computationally demanding for this Letter, these observations are strongly suggestive of a first-order transition. (In the Supplemental Material [43], we present results from simulations where we bias the Ag–Ag interaction that supports this notion.) This would further suggest a bcc-tet′ boundary in the P-T plane of the phase diagram. Termination of such a boundary at a critical point offers a possible explanation for the anomalous heat capacity, similar to the theory of Perrott and Fletcher [19].

In summary, our results suggest that for AgI at temperatures just above the superionic transition, a distorted tetragonal lattice of I^- competes with the bcc framework, which is accompanied by broken translational symmetry of the Ag^+ ions. This finding offers a potential mechanism for the experimentally observed memory effect, and may be relevant for the anomalous heat capacity at high temperatures. More broadly, order-disorder transitions are common in many ionic conductors [8], and whether these also underpin similar memory effects in other type I superionic conductors with stacking disordered low temperature phases remains an open question. While the machine learned representation of the PES that we employ is highly accurate, there are, of course, limitations on the accuracy of the underlying DFT functional (PBE + D3). For example, we observe a shift of the transition temperature in our simulations by approx. 70 K compared to experiment, and it is possible that the pressure is similarly offset. The experimental relevance of the intermediate structures observed just below the superionic transition temperature ($T \lesssim 330$ K) is also unclear at ambient pressure, and remains the topic of future study.

Notwithstanding such shortcomings, our observations appear in line with many curious experimental observations. The fine energy difference of a few meV/atom between the bcc and tetragonal structures suggests that, close to the transition temperature, both of these competing structures may be present in abundance. Further studies, both computational and experimental, are needed, however, to establish whether this is in the form of phase coexistence, or long-lived thermal fluctuations. Any such future work,

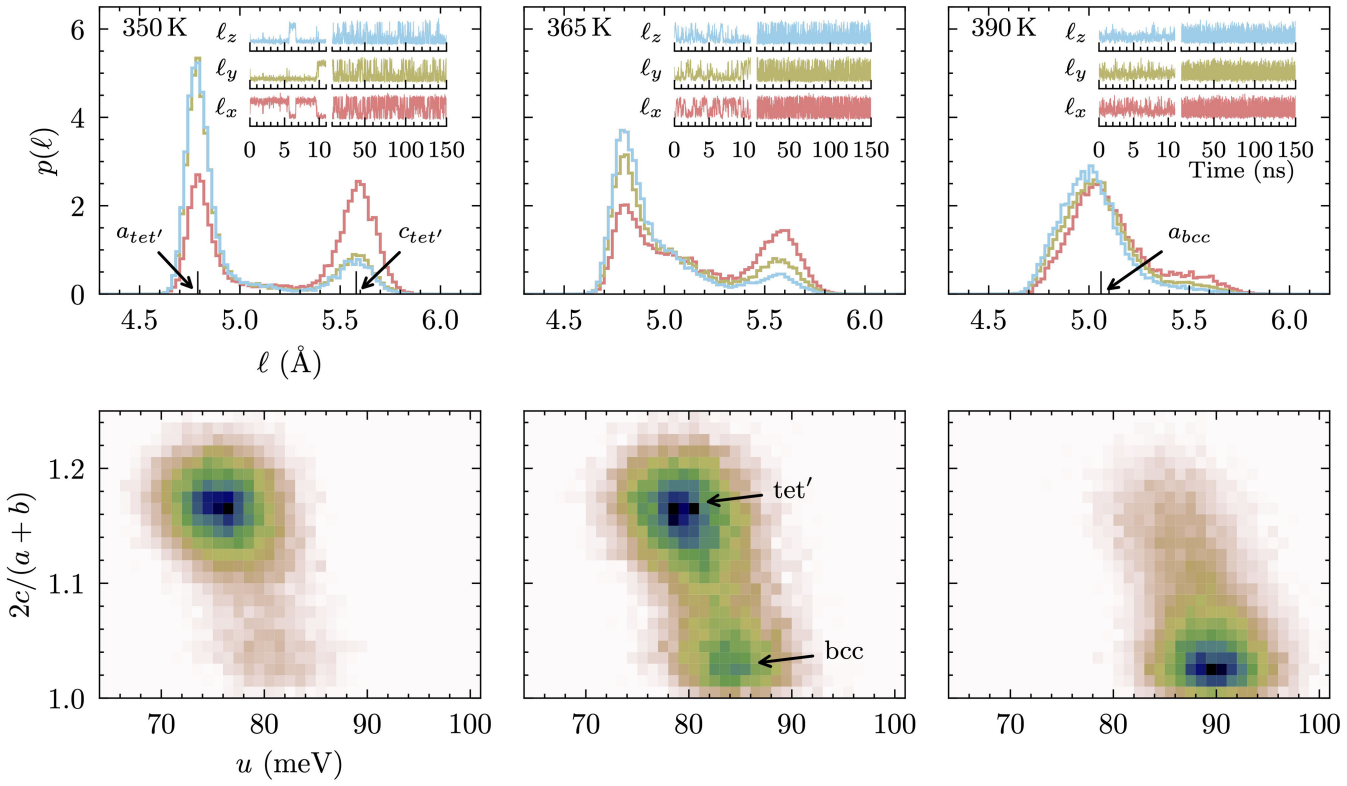

FIG. 3. The distorted tetragonal lattice exhibits long timescale fluctuations. Top panels show the probability density of $\ell_\nu = L_\nu/4$ (see text) with the trajectories shown in the insets (the first 10 ns is shown with a higher resolution to demonstrate anticorrelations). Although the symmetry axis flips between x, y, and z at 350 K (left) and 365 K (middle), the system remembers its initial condition. At 390 K (right) ℓ_x, ℓ_y, and ℓ_z are equivalent, although the distributions exhibit a fat tail. The lower panels show the joint probability densities for $2c/(a+b)$ (see text) and the potential energy per atom u. At 350 K we see that the tetragonal lattice dominates, with the bcc phase becoming more significant at 365 K. At 390 K, the bcc structure dominates. The tetragonal structure is approx. 5 meV/atom more stable than the bcc structure.

may also help to establish the relative abundance of these different structures, and shed light on the ionic transport mechanisms.

Acknowledgments—We thank Christoph Salzmann for helpful discussions. Access to CSD3 was obtained through a University of Cambridge EPSRC Core Equipment Award No. EP/X034712/1. S. J. C. is supported by a Royal Society University Research Fellowship (URF\R1\211144). W. B. and G. C. thank the AFRL for partial funding of this project through Grant No. FA8655-21-1-7010.

G. C. has an equity stake in the Symmetric Group LLP and Ångstrom AI Inc., companies engaged in the application of machine learning to material and molecular simulation.

[1] T. Famprikis, P. Canepa, J. A. Dawson, M. S. Islam, and C. Masquelier, Nat. Mater. **18**, 1278 (2019).
[2] S. Song, S. J. Park, M. Kim, J. S. Kim, B. J. Sung, S. Lee, J. H. Kim, and J. Sung, Proc. Natl. Acad. Sci. U.S.A. **116**, 12733 (2019).
[3] A. Marcolongo and N. Marzari, Phys. Rev. Mater. **1**, 025402 (2017).
[4] A. D. Poletayev, M. C. Hoffmann, J. A. Dawson, S. W. Teitelbaum, M. Trigo, M. S. Islam, and A. M. Lindenberg, Nature (London) **625**, 691 (2024).
[5] X. He, Y. Zhu, and Y. Mo, Nat. Commun. **8**, 15893 (2017).
[6] N. M. Vargas-Barbosa and B. Roling, Chem. Electro. Chem. **7**, 367 (2020).
[7] S. Muy, R. Schlem, Y. Shao-Horn, and W. G. Zeier, Adv. Energy Mater. **11**, 2002787 (2021).
[8] Y. Gao, A. M. Nolan, P. Du, Y. Wu, C. Yang, Q. Chen, Y. Mo, and S. H. Bo, Chem. Rev. **120**, 5954 (2020).
[9] S. Hull, Rep. Prog. Phys. **67**, 1233 (2004).
[10] V. Nield and W. Hayes, Defect Diffus. Forum **125–126**, 37 (1995).
[11] G. Burley, Am. Mineral. **48**, 1266 (1963).
[12] G. Burley, J. Chem. Phys. **38**, 2807 (1963).
[13] T. Takahashi, K. Kuwabara, and O. Yamamoto, J. Electrochem. Soc. **116**, 357 (1969).
[14] R. Bloch and H. Möller, Z. Phys. Chem. **152A**, 245 (1931).
[15] R. L. Smith, M. Vickers, M. Rosillo-Lopez, and C. G. Salzmann, Cryst. Growth Des. **19**, 2131 (2019).
[16] G. Burley, Acta Crystallogr. **23**, 1 (1967).

[17] C. M. Perrott and N. H. Fletcher, J. Chem. Phys. **48**, 2143 (1968).
[18] R. Vargas, Solid State Ionics **37**, 209 (1990).
[19] C. M. Perrott and N. H. Fletcher, J. Chem. Phys. **48**, 2681 (1968).
[20] A. Fontana, G. Mariotto, and M. P. Fontana, Phys. Rev. B **21**, 1102 (1980).
[21] G. Mariotto, A. Fontana, E. Cazzanelli, and M. P. Fontana, Phys. Status Solidi (b) **101**, 341 (1980).
[22] G. Mariotto, A. Fontana, E. Cazzanelli, F. Rocca, M. P. Fontana, V. Mazzacurati, and G. Signorelli, Phys. Rev. B **23**, 4782 (1981).
[23] V. Mazzacurati, G. Ruocco, G. Signorelli, E. Cazzanelli, A. Fontana, and G. Mariotto, Phys. Rev. B **26**, 2216 (1982).
[24] T. M. Brenner, C. Gehrmann, R. Korobko, T. Livneh, D. A. Egger, and O. Yaffe, Phys. Rev. Mater. **4**, 115402 (2020).
[25] P. Vashishta and A. Rahman, Phys. Rev. Lett. **40**, 1337 (1978).
[26] M. Parrinello, A. Rahman, and P. Vashishta, Phys. Rev. Lett. **50**, 1073 (1983).
[27] K. O'Sullivan, G. Chiarotti, and P. A. Madden, Phys. Rev. B **43**, 13536 (1991).
[28] P. A. Madden, K. F. O'Sullivan, and G. Chiarotti, Phys. Rev. B **45**, 10206 (1992).
[29] J. Tallon, Phys. Rev. Lett. **57**, 2427 (1986).
[30] J. L. Tallon, Phys. Rev. B **38**, 9069 (1988).
[31] R. Sato, K. Akagi, S. Takagi, K. Sau, K. Kisu, H. Li, and S. I. Orimo, J. Chem. Phys. **158**, 144116 (2023).
[32] B. C. Wood and N. Marzari, Phys. Rev. Lett. **97**, 166401 (2006).
[33] H. S. Dhattarwal, R. Somni, and R. C. Remsing, Nat. Commun. **15**, 121 (2024).
[34] A. P. Bartók, S. De, C. Poelking, N. Bernstein, J. R. Kermode, G. Csányi, and M. Ceriotti, Sci. Adv. **3**, e1701816 (2017).
[35] V. L. Deringer, A. P. Bartók, N. Bernstein, D. M. Wilkins, M. Ceriotti, and G. Csányi, Chem. Rev. **121**, 10073 (2021).
[36] J. P. Perdew, M. Ernzerhof, and K. Burke, J. Chem. Phys. **105**, 9982 (1996).
[37] S. Grimme, J. Antony, S. Ehrlich, and H. Krieg, J. Chem. Phys. **132**, 24103 (2010).
[38] E. R. Johnson and A. D. Becke, J. Chem. Phys. **123** (2005).
[39] P. Giannozzi *et al.*, J. Phys. Condens. Matter **21**, 395502 (2009).
[40] P. Giannozzi *et al.*, J. Phys. Condens. Matter **29**, 465901 (2017).
[41] P. Giannozzi, O. Baseggio, P. Bonfà, D. Brunato, R. Car, I. Carnimeo, C. Cavazzoni, S. de Gironcoli, P. Delugas, F. Ferrari Ruffino, A. Ferretti, N. Marzari, I. Timrov, A. Urru, and S. Baroni, J. Chem. Phys. **152**, 154105 (2020).
[42] A. Dal Corso, Comput. Mater. Sci. **95**, 337 (2014).
[43] See Supplemental Material at http://link.aps.org/supplemental/10.1103/PhysRevLett.134.026306 for more details on training and testing the MACE potential, spacegroup analysis of the iodine framework, further insights on cation distribution, partial structure factors, survival analysis of the superionic phases, and phase transitions induced by biasing the cation interactions, which also included Refs. [44–48].
[44] C. Schran, K. Brezina, and O. Marsalek, J. Chem. Phys. **153**, 104105 (2020).
[45] https://gitlab.com/amirhajibabaei/bulkagi.git.
[46] D. Mendels, J. McCarty, P. M. Piaggi, and M. Parrinello, J. Phys. Chem. C **122**, 1786 (2018).
[47] A. Togo, K. Shinohara, and I. Tanaka, Sci. Technol. Adv. Mater. **4**, 2384822 (2024).
[48] V. Ramasubramani, B. D. Dice, E. S. Harper, M. P. Spellings, J. A. Anderson, and S. C. Glotzer, Comput. Phys. Commun. **254**, 107275 (2020).
[49] I. Batatia, D. P. Kovacs, G. Simm, C. Ortner, and G. Csanyi, Adv. Neural Inf. Process. Syst. **35**, 11423 (2022).
[50] D. P. Kovács, I. Batatia, E. S. Arany, and G. Csányi, J. Chem. Phys. **159**, 044118 (2023).
[51] A. Jain, S. P. Ong, G. Hautier, W. Chen, W. D. Richards, S. Dacek, S. Cholia, D. Gunter, D. Skinner, G. Ceder, and K. A. Persson, Commentary: The materials project: A materials genome approach to accelerating materials innovation (2013), 10.1063/1.4812323.
[52] A. Hjorth Larsen *et al.*, The atomic simulation environment—A Python library for working with atoms (2017), 10.1088/1361-648X/aa680e.
[53] S. Melchionna, Phys. Rev. E **61**, 6165 (2000).
[54] A. Kvist and R. Tärneberg, Z. Naturforsch. A **25**, 257 (1970).
[55] These experimental values were obtained not by measuring electrical conductivity, but by tracking changes in the concentration of radioactive silver ions.
[56] A. F. Wright and B. E. F. Fender, J. Phys. C **10**, 2261 (1977).
[57] S. Hoshino, T. Sakuma, and Y. Fujii, Solid State Commun. **22**, 763 (1977).
[58] R. Cava, F. Reidinger, and B. Wuensch, Solid State Commun. **24**, 411 (1977).
[59] D. A. Keen, J. Phys. Condens. Matter **14**, 201 (2002).